Applied Physics A (2025) 131:909
https://doi.org/10.1007/s00339-025-09036-2

Applied Physics A
Materials Science & Processing

Advanced MXene/MoS_2 nanoparticles with polyethyleneimine intercalation for asymmetric energy storage applications

S. Sumathy[1] · M. Parthasarathy[1] · R. Suriakarthick[2] · V. Gowthami[1] · Amanullah Fatehmulla[3]

Received: 18 June 2025 / Accepted: 5 October 2025

Abstract

Titanium carbide (Ti_3C_2), a two-dimensional material known as MXene, is a promising electrode material for supercapacitors. Herein, MXene was synthesized by etching the Ti_3AlC_2 MAX phase, followed by intercalation with polyethyleneimine (PEI). Additionally, the precursor MoS_2 was injected into MXenes at an early stage. The MXene and MoS_2/MXene@PEI materials were characterized using X-ray diffraction, scanning electron microscopy, energy-dispersive X-ray spectroscopy, and BET analysis techniques. Several techniques were employed to assess the electrochemical properties of MXene, MoS_2/MXene, and MoS_2/MXene@PEI heterostructures. Based on the results of the electrochemical experiments, it has been demonstrated that the MoS_2/MXene@PEI NCs electrodes have the potential to achieve a maximum specific capacitance of 632 F g^{-1}. Additionally, the discharge current density of these electrodes is 1 A g^{-1}. Additionally, MoS_2 has been demonstrated to reduce the charge transfer resistance of MoS_2/MXene@PEI, as indicated by the results of electrochemical impedance testing. The electrochemical performance of MoS_2/MXene@PEI NCs was remarkable, particularly in terms of reversibility, cycle stability, and rate performance. The research concludes that MoS_2/MXene@PEI is an excellent candidate for use as an electrode in supercapacitors.

✉ M. Parthasarathy
mps2k7@gmail.com

[1] Department of Physics, School of Basic Sciences, Vels Institute of Science, Technology and Advanced Studies (VISTAS), Pallavaram, Chennai, Tamil Nādu 600 117, India

[2] Centre for Hybrid and Organic Solar Energy (CHOSE), University of Rome "Tor Vergata", via del Politecnico 1, Rome 00133, Italy

[3] Department of Physics and Astronomy, College of Science, King Saud University, Riyadh 11451, Saudi Arabia

Published online: 24 October 2025

Graphical Abstract

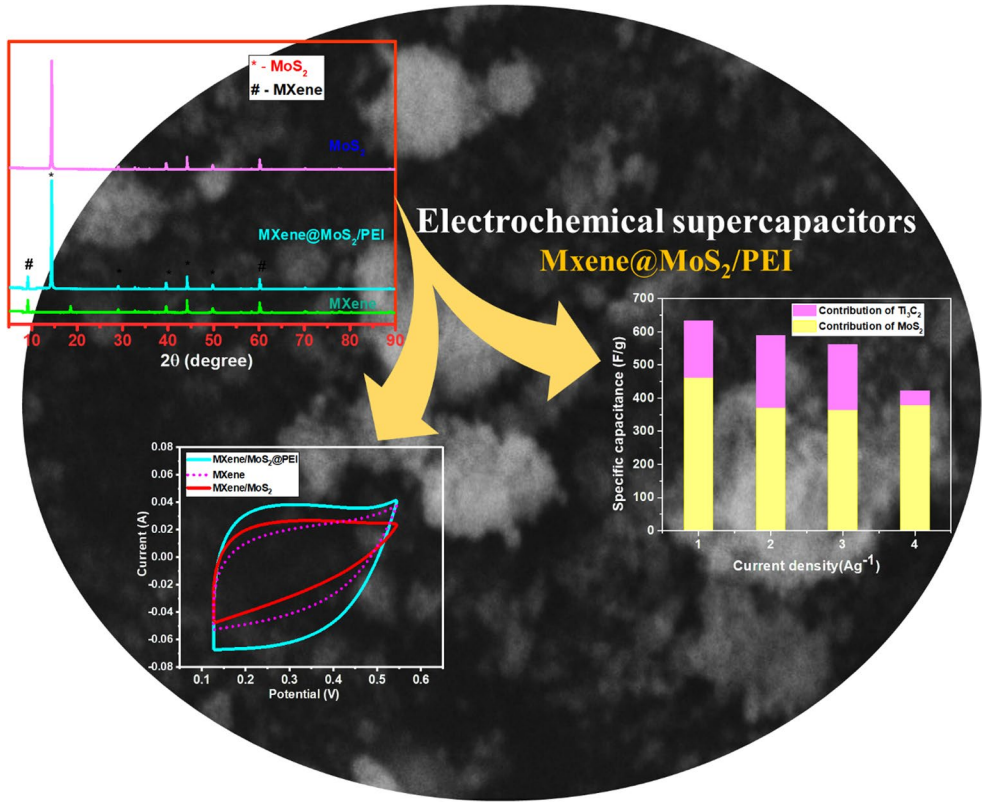

Highlights

- Successful synthesis of MoS2/MXene@PEI nanocomposite as a potential supercapacitor electrode.
- The presence of MoS2 inside the layers of MXene enhanced the specific surface area and capacitance.
- The MoS2/Mxene electrode has the maximum Csp of 632 F g−1 with the potential range of -0.08 V to 0.08 V.
- The electrochemical performance of MoS2/MXene was remarkable in terms of its reversibility, cycle stability, and rate performance.

Keywords MXene · MoS_2 · Nanocomposite · Supercapacitors · CV · GCD

1 Introduction

With the rising need for sustainable and renewable energy, modern applications in electronics, defense, and transportation demand highly efficient energy storage technologies [1, 2]. Among these, supercapacitors have gained significant attention because of their ability to deliver high power density and bridge the gap between conventional dielectric capacitors and rechargeable batteries [3, 4]. However, their relatively low energy density remains a key limitation [5–7]. Supercapacitors store and release energy through reversible ion adsorption at the electrode–electrolyte interface, functioning either as electrochemical double-layer capacitors (EDLCs) or pseudocapacitors depending on whether the process involves ion adsorption or faradaic redox reactions [8, 9].

Carbon-based materials such as graphene, carbon nanotubes (CNTs), and mesoporous carbons (CMKs) have been widely used as electrode materials due to their high conductivity and surface area [10, 11]. Yet, ongoing research seeks advanced materials with improved energy density and cycling stability. Two-dimensional transition metal carbides and nitrides, known as MXenes, have emerged as promising candidates. Derived from selective etching of the MAX phase, MXenes ($Mn_{+1}X_nT_x$) exhibit metallic conductivity, tunable surface terminations (–OH, –O, –F), and strong hydrophilicity, making them suitable for electrochemical energy storage [12, 13]. Their layered structure provides open channels for ion transport and excellent dispersibility

in both aqueous and organic solvents [14–19]. Molybdenum disulfide (MoS_2), a layered transition metal dichalcogenide with a graphene-like structure, also shows great potential in energy storage due to its high ionic conductivity, pseudocapacitive behavior, and charge storage capability [20]. Nevertheless, its limited conductivity hinders standalone performance. To address this, MXene/MoS_2 intercalated polyethyleneimine (PEI) heterostructures have been developed. In this design, MoS_2 nanosheets are confined between MXene layers, while PEI acts as a stabilizing polymer that prevents restacking, enhances dispersion, and introduces functional groups for ion interaction. This synergistic assembly enlarges interlayer spacing, boosts surface area and pore volume, and facilitates rapid ion transport, thereby improving electrochemical performance.

Polyethyleneimine (PEI) intercalated MoS_2/MXene nanocomposite frameworks play a crucial role in enhancing structural stability, electronic conductivity, and surface functionality of the hybrid system [21]. The positively charged amine groups of PEI interact electrostatically with the negatively charged surface of MXene and the layered MoS_2, effectively preventing nanosheet restacking and increasing interlayer spacing [22]. This enlarged interlayer distance improves ion diffusion and provides more accessible active sites for redox or photocatalytic reactions. Moreover, PEI introduces abundant functional groups (–NH_2, –NH–), which not only facilitate strong interfacial bonding between MoS_2 and MXene but also promote electron transfer by reducing charge recombination [21]. Unlike earlier MXene/MoS_2 combinations, our MoS_2/MXene@PEI composite integrates early-stage MoS_2 insertion with PEI intercalation, facilitating stable layer expansion, increased ion transport, and improved specific capacitance and cycle stability. As a result, the PEI-intercalated MoS_2/MXene framework exhibits improved electrochemical performance, catalytic activity, and stability compared to pristine MoS_2 or MXene alone.

Controlled in situ synthesis of MoS_2/MXene@PEI heterostructures has shown enhanced redox activity and broader voltage windows compared to pristine MXene or MoS_2. Notably, the MoS_2/MXene@PEI electrode in aqueous electrolytes exhibited a wide redox profile approaching 4.0 V, benefiting from the complementary features of both components. Moreover, organic electrolytes further extend the working voltage range, resulting in superior energy density [23–26]. Thus, MoS_2/MXene@PEI nanocomposites hold strong promise as next-generation supercapacitor electrodes, delivering high capacitance, extended voltage windows, and improved energy storage efficiency.

2 Experimental methods

2.1 Materials

Hangzhou Dayangchem Co., Ltd., located in India, provided the Ti_3AlC_2 (MAX Phase) (98%). Ammonium heptamolybdate $(NH_4)_6Mo_7O_{24}.4H_2O$), polyethyleneimine (PEI), polytetrafluoroethylene (PTFE), ammonium heptamolybdate (AHM), and carbon black were among the chemicals purchased from Sigma-Aldrich and used in their unpurified forms. SRL supplied DMSO, ammonium hydroxide, and hydrofluoric acid (40%).

2.2 Preparation of MXene

The preparation of MXene ($Ti_3C_2T_x$) from the MAX phase involved dissolving 2 g of LiF in 20 mL of 9 M HCl with continuous stirring for 30 min, after which 2 g of MAX precursor was carefully added. The etching process was conducted in a PTFE reactor at 37 °C with stirring maintained at 400 rpm for 24 h. The obtained mixture was then subjected to repeated centrifugation with deionized water (4000 rpm, 10 min) until the pH was greater than 6. For intercalation, ethanol pre-treated with argon was introduced, followed by ultrasonic treatment for 1 h. The resulting solid was redispersed in deionized water, centrifuged, and the supernatant was collected and preserved at 5 °C for later use.

2.3 Synthesis of MXene/MoS_2@PEI NCs

The MXene/MoS_2–intercalated polyethyleneimine (PEI) nanocomposites were prepared by dissolving an appropriate amount of ammonium heptamolybdate in 60 mL of ammonium hydroxide along with 5 mL of deionized water to obtain a homogeneous precursor solution. This solution was exposed to H_2S gas at 25 °C for 1 h with constant stirring, and subsequently heated to 60 °C until a deep red colour developed, confirming the formation of MoS_x species. In parallel, MXene was dispersed in 20 mL of ethylene glycol to form a stable slurry, which was then introduced into the warm MoS_x suspension to promote the nucleation and deposition of MoS_2 on the MXene layers. After cooling to room temperature, the composite was subjected to incipient-wetness impregnation with 0.1 M polyethyleneimine, during which the poly-MXene displayed a characteristic dark red colour, indicating successful intercalation and adsorption of PEI. The obtained material was separated by centrifugation, thoroughly washed to eliminate unbound species, dried, and finally calcined at 300 °C in a nitrogen environment to yield the MXene/MoS_2@PEI nanocomposites.

2.4 Electrochemical measurement

A slurry was prepared by mixing MXene and/or MoS_2/MXene@PEI nanocomposite with acetylene black and poly(tetrafluoroethylene) in an 8:1:1 weight ratio, followed by ultrasonication in N-methyl-2-pyrrolidone (NMP) to form a homogeneous electrode paste. The slurry was coated onto 1 cm^2 GraFoil paper and dried to fabricate the working electrode, with approximately 1.5 mg of active material. The electrochemical performance was evaluated using cyclic voltammetry (CV), galvanostatic charge–discharge (GCD), and electrochemical impedance spectroscopy (EIS) on a Biologic SP-240 workstation in a symmetric two-electrode configuration with 1 M H_2SO_4 as the electrolyte. The fabricated electrodes demonstrated high specific capacitance with excellent rate capability, delivering stable charge–discharge characteristics over prolonged cycling. Furthermore, the nanocomposite exhibited superior energy density while maintaining robust cycling stability, indicating its potential as an efficient electrode material for next-generation energy storage devices.

3 Results and discussions

3.1 XRD analysis

The XRD patterns of MXene, MoS_2, and MoS_2/MXene@PEI nanocomposites are presented to illustrate their structural characteristics. For the MAX phase, diffraction peaks were observed at 2θ values of 9.2°, 19.2°, 34.0°, 36.7°, 39.0°, 41.8°, 48.5°, 52.4°, 56.6°, 60.2°, 65.6°, 70.5°, and 74.1°, corresponding to the (002), (004), (100), (103), (104), (105), (107), (108), (109), (110), (1011), (118), and (1013) planes, respectively (Fig. 1a). After thermal treatment, the (002) and (004) peaks at 9.2° and 19.2° shifted to lower angles, indicating an expansion in the interlayer spacing caused by the removal of Al layers during etching. Additionally, the disappearance of non-basal reflections around 39° further confirmed the successful formation of MXene [27]. The diffraction peaks associated with the (001), (002), (004), and (0010) planes broadened and shifted to lower angles, validating aluminium removal and MXene generation. A few weak peaks at 25°, 37°, and 47° were also detected, attributed to traces of partially oxidized TiO_2. For MoS_2, the reflections matched with JCPDS Card No. 03–065-0160 [28], with peaks corresponding to the (002), (100), (103), and (105) planes. The presence of weaker intensity peaks at 2θ values of 33.8°, 39.4°, and 57.1° corresponded to the (100), (103), and (110) planes, confirming MoS_2 intercalation between MXene layers. However, in the MoS_2/MXene@PEI nanocomposites, the MoS_2 reflections became less distinct due to their nanostructured integration with MXene. Peaks at 14.38° (002) and 33.12° (100), consistent with JCPDS Card No. 29–0101 for MXene, indicated increased interlayer spacing, as evidenced by the reduced intensity of the (002) peak in the nanocomposite compared to pristine MXene, reflecting the confinement of MoS_2 within the MXene layers [29, 30].

3.2 BET surface area analysis

The pore size distribution and N_2 adsorption–desorption isotherms of MoS_2/MXene@PEI nanocomposites and pure MXene are presented here. The isotherm of MXene exhibits characteristics of a Type IV curve with an H3 hysteresis loop, confirming the coexistence of mesopores and slit-shaped pores, which arise from the layered structures

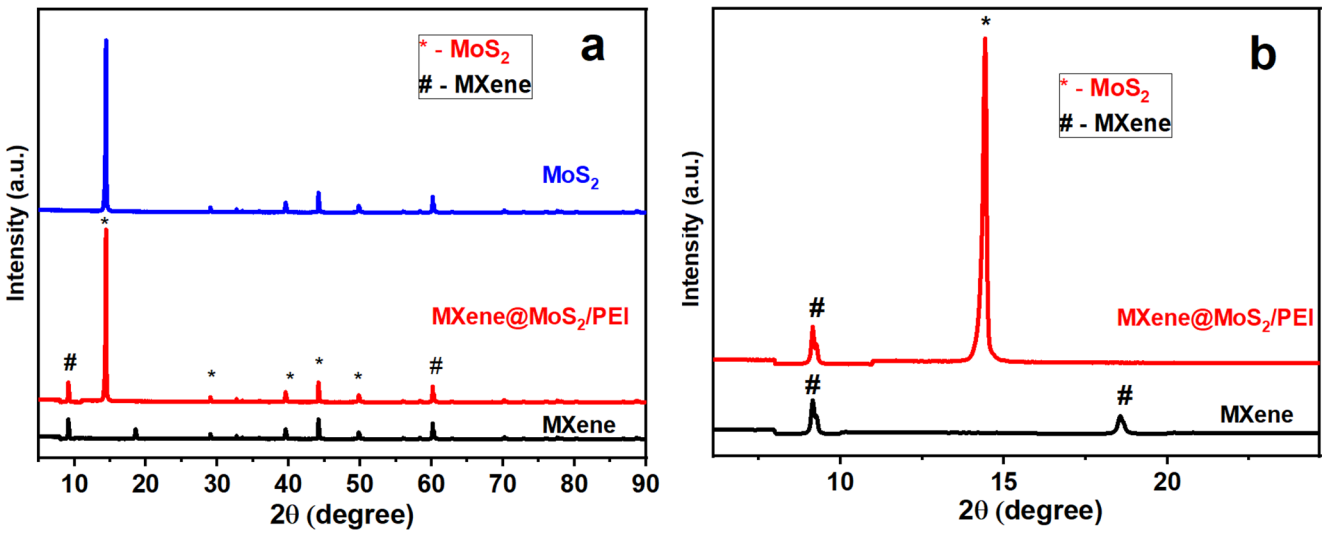

Fig. 1 (**a**) XRD pattern of MoS_2, MXene, MoS_2/MXene@PEI NCs, and (**b**) magnified image of XRD pattern

of both MXene and MoS_2. The BET analysis revealed that MXene possesses a specific surface area of 60.12 m^2/g, while MoS_2/MXene@PEI shows a significantly higher value of 113.30 m^2/g, attributed to the incorporation of MoS_2 within the MXene interlayers. Similarly, the pore volume of MXene was measured at 0.022 cm^3/g, in contrast to 0.076 cm^3/g for MoS_2/MXene@PEI, further demonstrating the enhancement provided by MoS_2 loading. As illustrated in Fig. 2, the increased surface area and pore volume of the composite facilitate improved electrode–electrolyte interaction, thereby contributing to superior electrochemical performance compared to pristine MXene.

3.3 Morphological analysis

Due to the availability of intercalation sites and the decrease in ion diffusion paths, the two-dimensional poly-heterostructures are visible in Fig. 3a and b. The layered MXene and MXene@MoS_2@PEI crystal structure is suitable for improving the supercapacitive performance of the material. These scanning electron micrographs of MXene@MoS_2@PEI NCs show that the MoS_2 layers are formed on top of the MXene layers, effectively concealing the accordion-like structures within the MXene. Confirmation of the formation and existence of MoS_2 on the surface of MXene is provided by the elemental mapping analysis of MXene@MoS_2@PEI. This analysis reveals the presence of C (Fig. 3c), Ti (Fig. 3d), Mo (Fig. 3e), and S (Fig. 3f) as the primary elements.

3.4 HRTEM/SAED analysis

Further confirmation of the **MXene@MoS_2**@PEI heterostructure nanocomposites was obtained through transmission electron microscopy (TEM) and high-resolution TEM (HRTEM), which provided insights into both the morphology and lattice spacing (Fig. 4a and b). The crystalline nanostructures revealed the coexistence of Ti_3C_2 and MoS_2 within the heterostructure, showing distinct lattice spacings of 0.26 nm and 0.67 nm, corresponding to the (103) plane of Ti_3C_2 and the (002) plane of MoS_2, respectively (Fig. 4c). The observed lattice expansion is attributed to the intercalation of polyethyleneimine (PEI), whose long-chain, amine-rich structure can penetrate between adjacent MXene and MoS_2 layers. The abundant $–NH_2$ groups of PEI form electrostatic interactions and hydrogen bonds with negatively charged surface terminations (–O, –OH, –F) on MXene, while also interacting with sulfur atoms in MoS_2. This dual interaction prevents layer restacking, increases interlayer spacing, and creates additional ion-diffusion channels. Consequently, the intercalation of PEI not only stabilizes the heterostructure but also enhances its electrochemical performance by facilitating faster ion transport and improving electrode–electrolyte accessibility.

By carrying out selected area electron diffraction (SAED) on the MoS_2/MXene@PEI heterostructure, we were finally able to demonstrate that the synthesis of the MoS_2/MXene@PEI nanocomposites was successful (Fig. 4d-f). In accordance with the reported findings, the diffraction rings were observed for Ti_3C_2 (103) and MoS_2 (101). It is essential to note that the unique distribution design of MoS2/MXene@PEI NCs can potentially facilitate energy conversion, storage, and fingerprinting. This is because it grants the ability to ionise tiny molecules more efficiently.

3.5 Electrochemical behavior

Cyclic voltammetry and a symmetric two-electrode arrangement were used to analyse the electrochemical performance

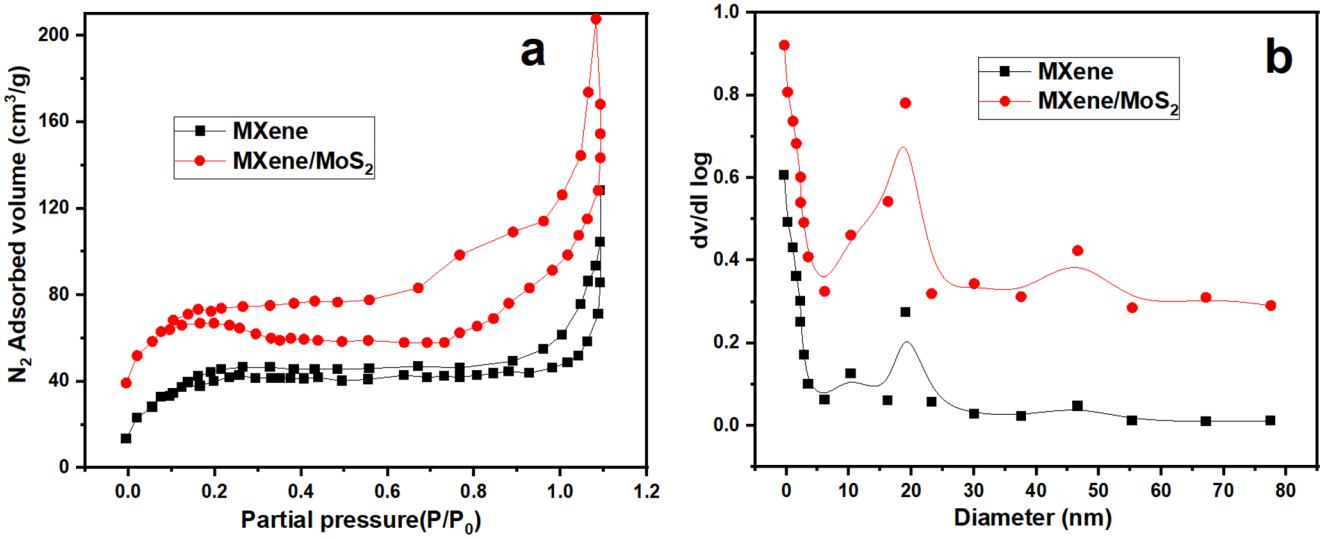

Fig. 2 (**a**) BET Analysis (**b**) pore size distribution of MXene, and MoS_2/MXene

of MXene and MXene@MoS_2@PEI. An investigation was conducted using hydrogen sulfide at a concentration of 1 M H_2SO_4 as the electrolyte. The cyclic voltammogram of MXene@MoS_2@PEI is shown in Fig. 5a for your viewing pleasure. The potential window range includes 0.1 V to 0.6 V, encompassing this voltammogram. Figure 5a shows the same outcomes for MXene at voltages of 10, 20, 60, and 100 millivolts per second. The semi-rectangular CV responses of MXene, MXene@MoS_2, and MXene@MoS_2/PEI NCs demonstrate the remarkable capacitive performance of these materials [31, 32]. With an electrolyte composed of MoS_2/MXene@PEI NCs in aqueous H_2SO_4 and a cell voltage of approximately 1 V, a window of opportunity for oxidation and reduction is created. Electrolyte aqueous solutions typically have a cell voltage of around 1 V, while organic electrolytes often have a voltage ranging from 3 to 3.5 volts. MXene@MoS_2/PEI electrodes are excellent for strong applications because of the synergistic interaction between the two materials, which broadens the potential window. This makes the electrodes ideal for use in a variety of applications. The absence of oxidation or reduction peaks in the CV response when the scan rate was raised provides evidence that the MXene, MXene@MoS_2, and MXene@MoS_2/PEI NCs electrodes maintain a charging and discharging rate that is pseudo-constant throughout the cycle. The substantial increase in scan rates showed this. However, the CV curve for MXene, MXene@MoS_2, and MXene@MoS_2/PEI NCs continues to exhibit a standard semi-rectangle behavior, even though it becomes more pronounced as the scan rate increases. Everything you have indicated regarding each of these compounds is correct. Based on the findings, it can be concluded that both of the materials exhibit electrochemical stability when subjected to high potentials. Even though the scan rate is increased, the material's stability at high potentials may be maintained due to the resistance that MoS_2 provides.

This occurs because the resistance leads to a significant reduction in the effective contact between the ions and the electrode. It is evident from the data shown in Fig. 5b that the regions of the CV curves for MXene, MXene@MoS_2, and MXene@MoS_2/PEI NCs electrodes are distinct, indicating that the specific capacitance of the former is significantly higher. This phenomenon may be explained by the fact that MXene and MoS_2 are composed of complementary components. After being encased in MXene, the stacking of MoS_2 begins immediately upon enclosure. Combining the two materials enables the achievement of a higher number of reversible activity sites, lower internal resistance, and enhanced ion transfer and pseudo-capacitance measurements. Figure 5c compares the CV profiles of MXene, MXene@MoS_2, and MXene@MoS_2/PEI at 100 mV s^{-1}. Among them, MXene@MoS_2/PEI shows the largest enclosed area, suggesting its superior capacitive

Fig. 4 (**a**) TEM image, (**b**) HRTEM image, (**c**) SAED pattern of MXene@polyamine, (**d**) TEM photograph, (**e**) HRTEM, (**f**) SAED pattern of MoS_2/MXene@PEI nanocomposites

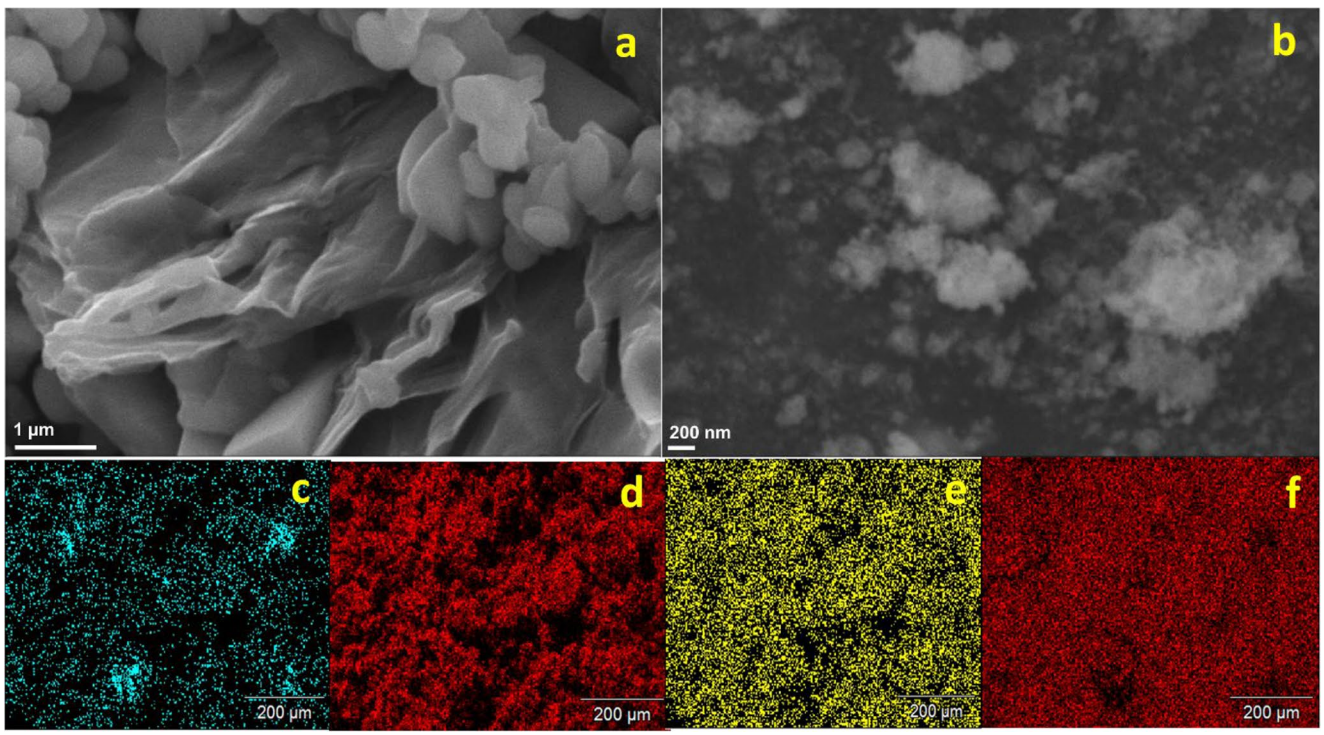

Fig. 3 SEM Analysis of (**a**) MXene, (**b**) MXene@MoS_2, (**c-f**) elemental mapping analysis of MXene@MoS_2 nanoparticles

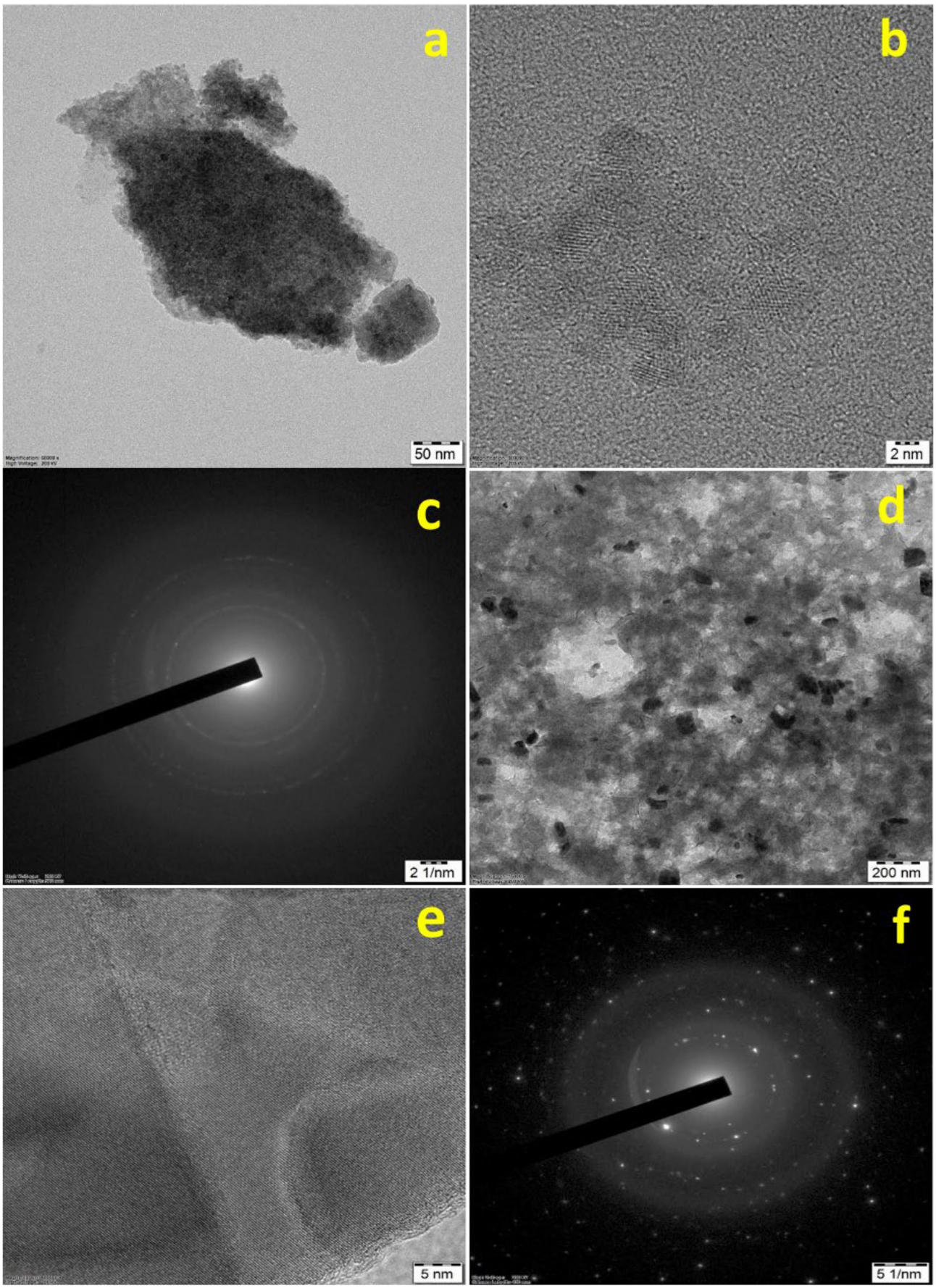
a
50 nm
b
2 nm
c
2 1/nm
d
200 nm
e
5 nm
f
5 1/nm

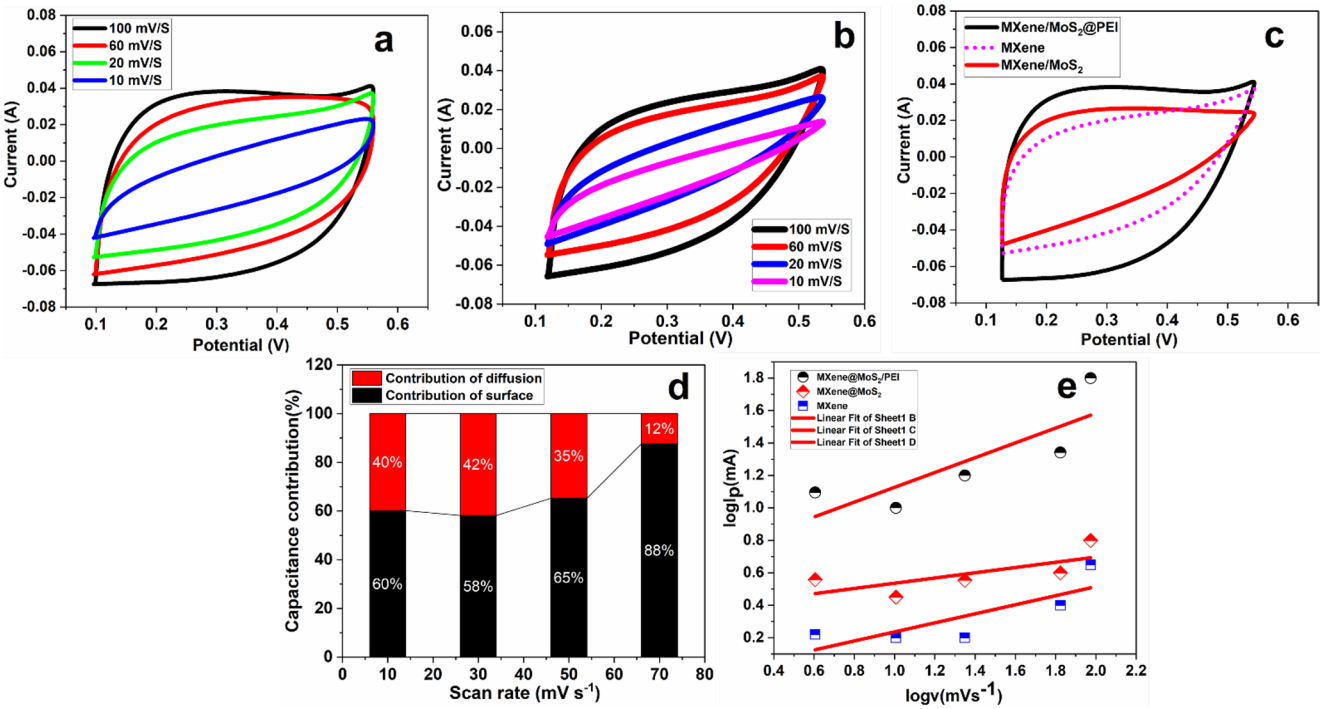

Fig. 5 (**a**) CV graph of multi-scan rate of MXene@MoS_2/PEI NCs (**b**) CV graph of MXene and MAX phase (**c**) comparable analysis of MXene, MXene@MoS_2, and MXene@MoS_2/PEI NCs (**d**) cathodic peak current density (**e**) capacitance contribution with different scan rates

performance. The enhancement arises from the synergistic effect of MXene's conductive layers and MoS_2 nanosheets intercalated with PEI, which together provide additional active sites, improved ion diffusion pathways, and reduced internal resistance.

The cathodic peak current density depends on the scanning rate to calculate the b-values of MoS_2 and MAX. As can be seen in the Fig. 5d, the MoS_2 electrode exhibits rapid electrochemical reaction kinetics due to a bias in the capacitance, but the MAX electrode exhibits kinetics of 0.62. Because of this preconception, the response turned out to be relatively prompt. Surface-controlled capacitance is considered more significant in the interaction between the two than diffusion-controlled capacitance, as stated by this bias. To measure the surface-controlled capacitance in scan rate-dependent analysis with a fixed voltage, the equation,

$$I(V) = K_1(V) + K_2(V)^{1/2} \quad (1)$$

The symbols k_1 and k_2 may indicate the diffusion-controlled processes, respectively. Several different scan speeds were used to investigate the capacitance contribution of the MAX electrode, as shown in Fig. 5e. The contribution of diffusion- and surface-controlled charge storage. At 10 mV s^{-1}, surface-controlled capacitance contributes about 60%, while diffusion accounts for 40%. As the scan rate increases to 70 mV s^{-1}, surface-controlled processes dominate (88%), highlighting the excellent capacitive nature and fast charge transport of the MXene@MoS_2/PEI electrode, which indicates that this feature is more significant than the diffusion-controlled capacitance. Because MoS_2 and MXene are both two-dimensional, they have a high basal surface area. This implies that they can retain sufficient electrolyte ions to fuel the electrochemical process.

3.6 GCD analysis

To achieve all these objectives, the two materials work in collaboration. GCD measurements were used to evaluate the specific capacitance of MXene and MoS_2/MXene@PEI NCs, as seen in the Figure. 6a and b. The GCD curves of MXene@MoS_2/PEI nanocomposites (NCs), pristine MXene, and MXene@MoS_2 binary composites at various current densities are presented in Fig. 6a and b. These charge–discharge profiles were recorded at current densities ranging from 1.0 to 4.0 A g^{-1}, as shown in Fig. 6a and b. The authors declare that they have no known competing financial interests or personal relationships that could have appeared to influence the work reported in this paper. while the comparative performance of the different electrode systems is given in Fig. 6c. The nearly symmetrical triangular shapes observed in the charge–discharge profiles of MXene@MoS_2/PEI NCs and MXene highlight their superior capacitive nature, indicating efficient, reversible

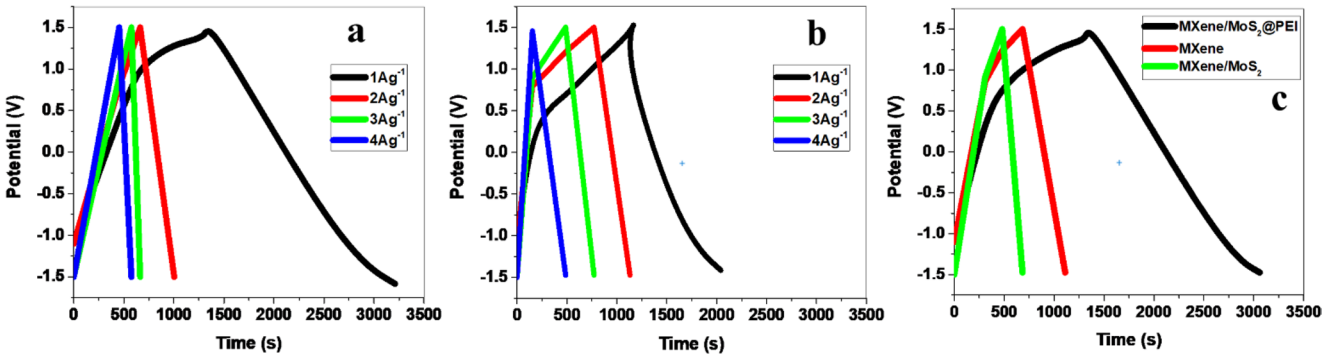

Fig. 6 (**a**) GCD pattern of MoS_2/MXene@PEI NCs (**b**) GCD pattern of MXene (**c**) GCD graph of Comparable analysis of MXene, MXene@MoS_2, and MXene@MoS_2/PEI NCs

faradaic reactions and a nearly linear potential–time relationship. It is possible to use the formula to determine the electrode's specific capacitance (C_{sp}).

$$C_{sp} = \frac{I \times \Delta t}{m + \Delta V} \tag{2}$$

At higher current densities (1–4 A g^{-1}), the GCD curves of MXene@MoS_2/PEI NCs (Fig. 6a) retain their symmetrical shape with minimal IR drop, revealing the synergistic effect of double-layer capacitance from MXene layers and pseudocapacitance contributions from MoS_2 and PEI. Such behavior confirms the role of binary and ternary composites in lowering resistance, enhancing ion accessibility, and stabilizing charge–discharge processes.

The calculated specific capacitances of MXene@MoS_2/PEI NCs are 632, 589, 562, and 422 F g^{-1} at 1, 2, 3, and 4 A g^{-1}, respectively, while pristine MXene delivers lower capacitances of 462, 372, 365, and 380 F g^{-1} at the same current densities (Fig. 6a **and b**). At 1 A g^{-1}, the MXene@MoS_2/PEI NCs show a longer discharge time than MXene alone, directly reflecting their higher capacitance and better charge storage ability. This enhancement can be attributed to improved ion transport pathways and interfacial contact between MoS_2 and MXene layers, facilitated by the PEI network. As observed in Fig. 6c, the ternary MXene@MoS_2/PEI NCs outperform both MXene and MXene@MoS_2 binary composites, owing to their higher surface area, shortened diffusion paths, and superior electron transfer kinetics. These results confirm that the innovative composite design enhances electrochemical performance, allowing simultaneous contributions from EDL capacitance and pseudocapacitance, thereby maximizing the overall charge storage capacity.

The electrochemical performance of MoS_2/MXene@PEI was evaluated through impedance spectroscopy, cyclic voltammetry, and specific capacitance analysis, as illustrated in Fig. 7. The Nyquist plots (Fig. 7a) demonstrate a significant difference in impedance behavior between pristine MXene and the MoS_2/MXene@PEI composite. The semicircle observed in the high-frequency region corresponds to charge transfer resistance (R_{ct}), while the nearly vertical line in the low-frequency region represents ideal capacitive behavior governed by Warburg diffusion. The pristine MXene electrode exhibited a higher equivalent series resistance ($R_s \approx 125\ \Omega\ cm^{-2}$), whereas MoS_2/MXene@PEI showed a lower R_s value of ~88 $\Omega\ cm^{-2}$. This reduction indicates improved electrical conductivity and

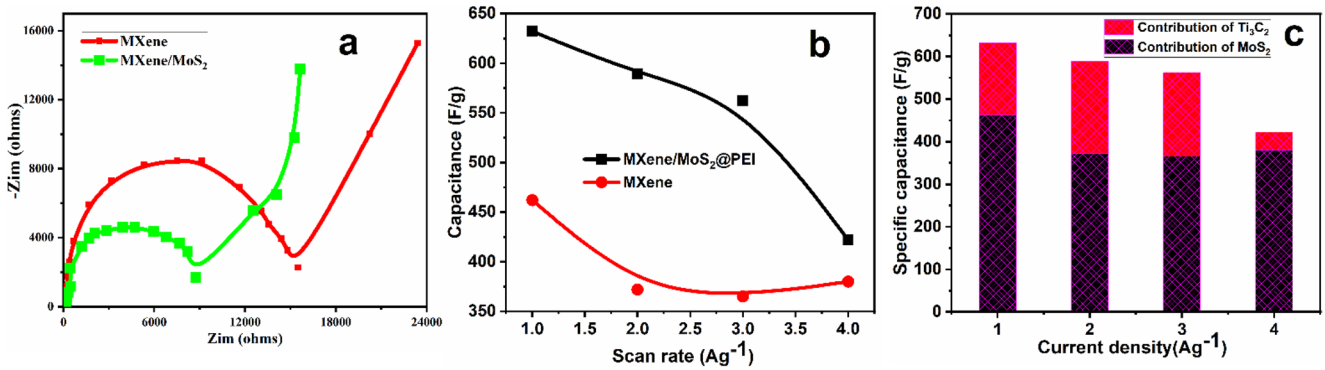

Fig. 7 (**a**) EIS analysis of MXene, MXene@MoS_2, and MXene@MoS_2/PEI NCs (**b**) comparison of capacitance (**c**) capacitance contribution of MoS_2 and MXene plot

ion transport pathways due to the synergistic integration of MoS_2 nanosheets and the polyamine network (PEI), which facilitates rapid charge transfer and electrolyte diffusion.

Capacitance retention with respect to scan rate is shown in Fig. 7b. The MoS_2/MXene@PEI composite delivered the highest specific capacitance (~620 F g^{-1} at 1 A g^{-1}), outperforming both pristine MXene and MoS_2/MXene without PEI. Even at higher current densities (4 A g^{-1}), the composite retained superior capacitance, highlighting its excellent rate capability. The improved performance can be ascribed to the conductive MXene scaffold, the redox-active MoS_2 layers, and the PEI framework that prevents nanosheet restacking while enhancing electrolyte accessibility. Also, the augmented surface area of MoS_2/MXene@PEI offers more accessibility to active sites for ion adsorption and promotes electrolyte infiltration, hence directly improving the specific capacitance of the electrode. The relative contributions of capacitive and diffusion-controlled processes are presented in Fig. 7c. At lower current densities, capacitive contributions dominate, whereas with increasing current density, the diffusion-controlled contribution becomes more significant, confirming the pseudocapacitive nature of the composite. This dual contribution mechanism ensures both high energy density and excellent rate capability, in agreement with earlier reports on hybrid supercapacitor materials. In MXene-based composites, PEI provides distinct benefits over widely used conductive polymers including polyaniline (PANI), polypyrrole (PPy), and poly(3,4-ethylenedioxythiophene) (PEDOT). While conductive polymers might boost conductivity, they often suffer from difficulties such weak long-term cycling stability and volumetric changes during repetitive charge–discharge processes [33]. For instance, PANI and PPy have been found to display low cycle life and capacity retention attributed to their intrinsic structural instability. The interaction between PEI and MXene surfaces is robust, effectively preventing layer restacking and facilitating stable interlayer expansion [34, 35]. This material exhibits chemical stability, can be processed in aqueous environments, and promotes ion transport while maintaining the conductivity of MXene, thereby enhancing the electrochemical performance of MoS_2/MXene@PEI.

Figure 8 illustrates that the MoS_2/MXene@PEI nanocomposite electrodes have maintained their stability after several cycles. The rapid increase in specific capacity was

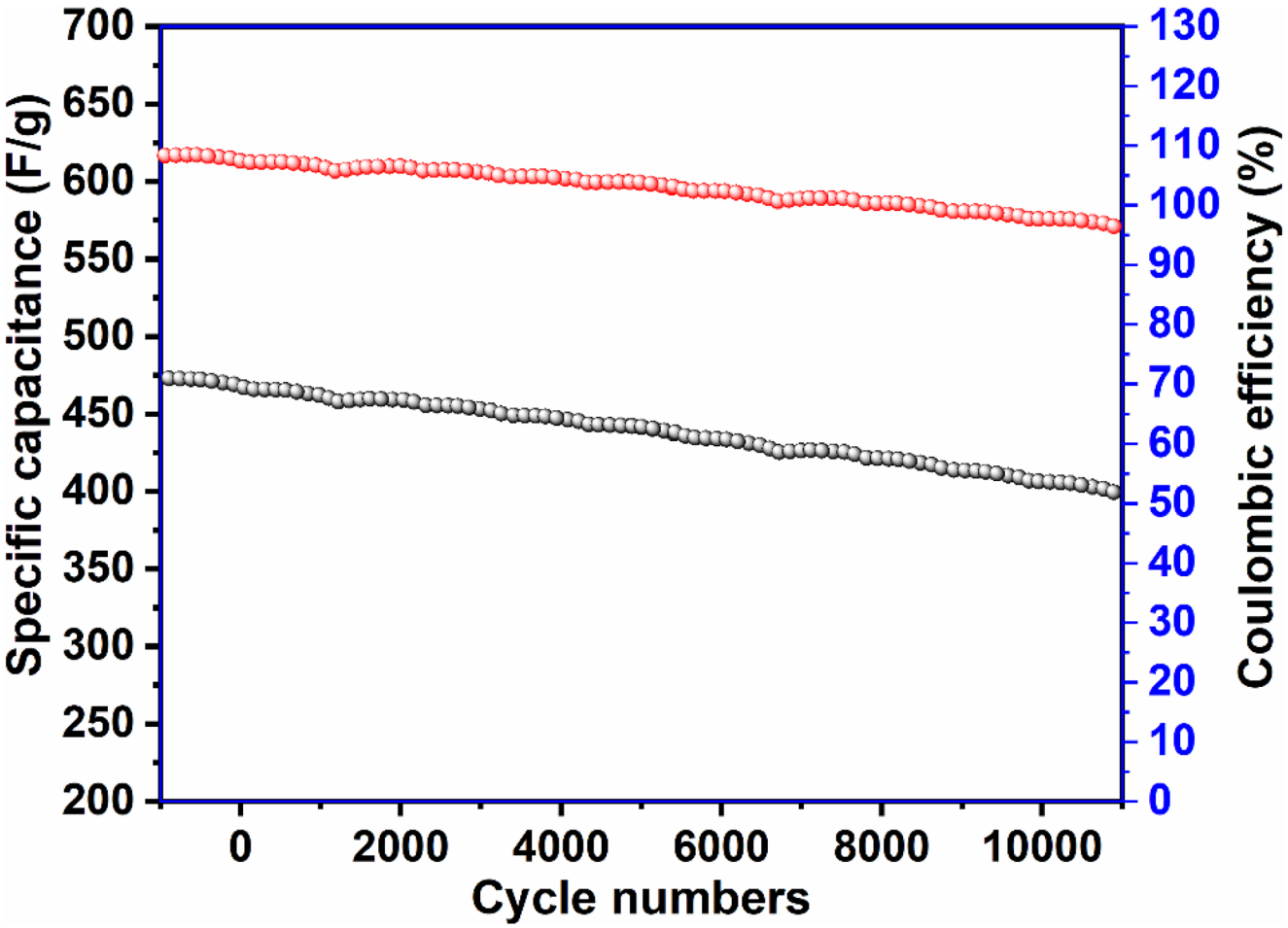

Fig. 8 Cycling stability analysis of MXene and MoS_2/MXene@PEI NCs

attributed to the activation of active materials during the initial cycles. Following 10,000 cycles, the MoS_2/MXene@PEI electrode maintains a discharge capacity that is significantly superior to that of other materials. At a current density of 4 A g^{-1}, it has been shown that after 10,000 cycles, over 96% of the Columbia efficiency remains intact. The reduction in resistance value after 10,000 cycles indicates a substantial enhancement in the conductivity of MoS_2/MXene@PEI NCs. The electrode material MoS_2/MXene@PEI NCs may be used in the development of long-term storage systems owing to its inherent stability.

After 10,000 cycles, the stability of the MoS_2/MXene@PEI structures is not compromised, even when they are exposed to a high current density of 4 A g^{-1}. This is demonstrated by the remarkable rate performance and the fact that MoS_2 is embedded within the MXene layers, providing evidence. Figure 9 shows the charge rates of 1, 2, 3, and 4 A g^{-1} alongside the Ragone plot of MXene and MoS_2/MXene@PEI NCs. To calculate the energy density E (in watt-hours per kilogram) and the power density P (in watts per kilogram) based on the galvanostatic charge-discharge data, the following equations may be utilised: Following the multiplication of E by 3600 and the subsequent division of the resulting value by Δt, the letter P is the outcome.

The potential window for discharge is marked by V(ŸV), and the discharge time is represented by the symbol Ÿt (s). According to the findings, the Ragon plot is seen in the **Figure. 9**. The most incredible power density was 1200 W kg^{-1} when the energy density range was 90 W h kg^{-1} for MoS_2/MXene@PEI NCs and 90 W h kg^{-1} and power density was 800 W kg^{-1} for MXene. This was achieved at a charging rate of 1 A g^{-1}. Regarding electrode material, MoS_2/MXene@PEI NCs is an excellent choice because of its high energy density and power output. A density of 90 W h kg^{-1} applies to it.

4 Conclusion

Following the novel fabrication of MXene and polyamine during the MAX phase, heterostructures A consisting of MXene/MoS_2@PEI NCs were created effectively using the incipient wetness impregnation method. X-ray diffraction (XRD) tests demonstrated that aluminium was successfully

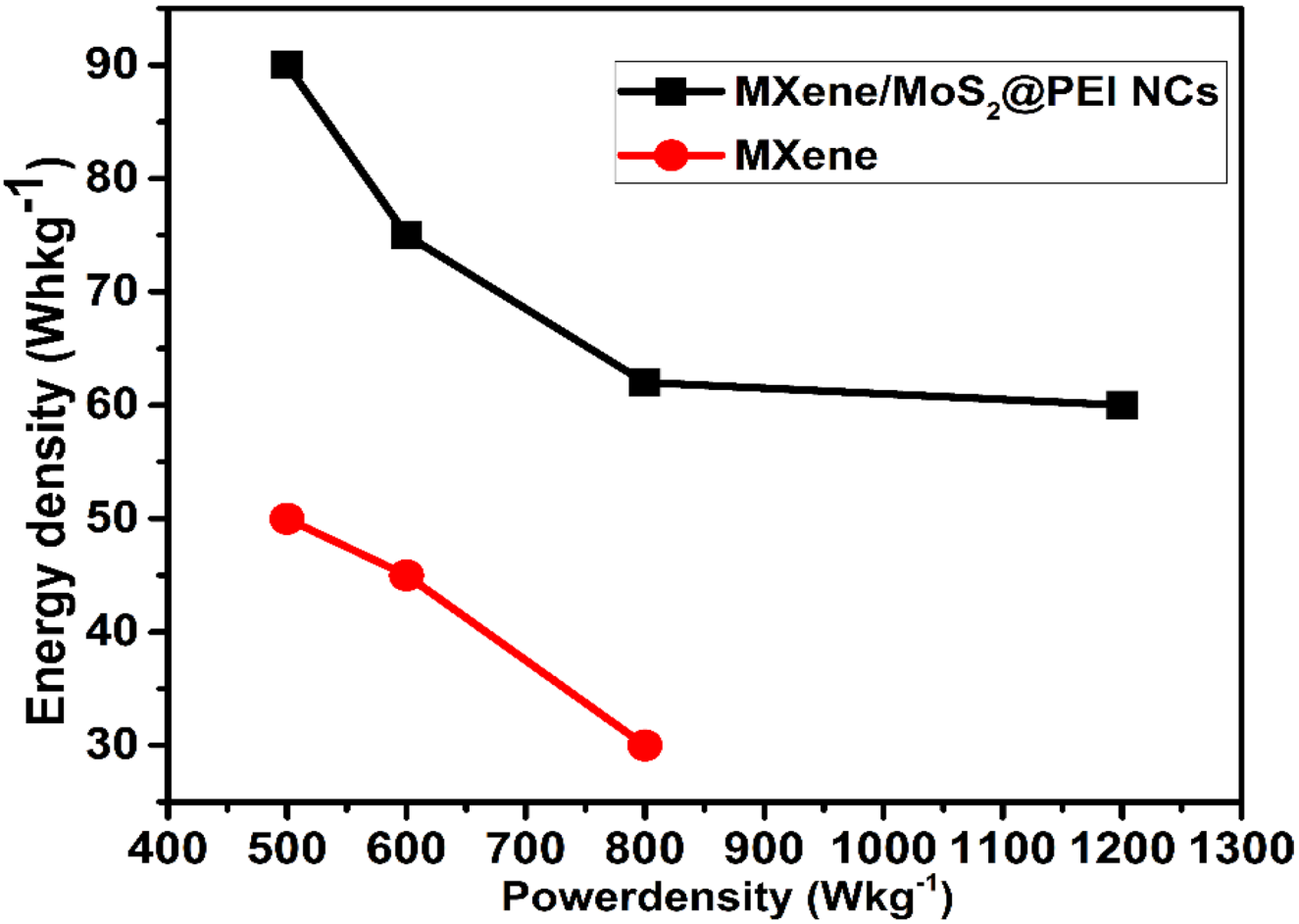

Fig. 9 Ragon plot of Energy density vs. Power density of MXene and MXene/MoS_2@PEI NCs

removed from the MAX phase and that multilayer MXene was produced. By employing SEM-EDX mapping, it was possible to prove that multilayer MXene was formed and that MoS_2 was integrated into these layers. This was a practical demonstration. In addition, the BET analysis revealed that incorporating MoS_2 into MXene led to a proportional change in the surface area and pore volume of the MoS_2/MXene@PEI NCs material. In the form of a well-defined CV response with a quasi-rectangular shape, MXene and MXene/MoS_2@PEI NCs exhibited behaviour characteristic of a pseudo-capacitor. The specific capacitance of MoS_2/MXene@PEI NCs was measured to be 632 F g^{-1} at a current density of 1 A g^{-1}. This was the highest specific capacitance ever recorded. GCD analysis was used to demonstrate this point. It was established using GCD and impedance spectroscopy that MXene/MoS_2@PEI NCs have very stable cycling properties and extremely high electrical resistance. MoS_2 and polyamine are added to MXene/MoS_2@PEI NCs, which results in a decrease in the material's equivalent series resistance. The impedance data indicate that the internal resistance decreases after 10,000 cycles, and the GCD data demonstrate that the discharge time of MoS_2/MXene@PEI remains more than 96% even after such a large number of cycles. These findings suggest that polyamine-intercalated MXene/MoS_2 is an outstanding electrode material that is attractive for long-term energy storage devices. The MXene/MoS_2@PEI polyheterostructure demonstrates potential as an effective electrode material for supercapacitors.

Acknowledgements One of the authors, Mrs. S. Sumathy, expresses her gratitude to the Vels Institute of Science, Technology and Advanced Studies (VISTAS), Pallavaram, Chennai-600117, for their support in conducting this research. The author (Amanullah Fatehmulla) extend their appreciation to Ongoing Research Funding Program, (ORF-2025-1041), King Saud University, Riyadh, Saudi Arabia, for financial assistance.

Author contributions S Sumathy: Writing– original draft, Visualization, Methodology, Investigation, Formal analysis, Data curation, Conceptualization. M. Parthasarathy: Writing– original draft, Validation, Supervision, Investigation, Methodology, Conceptualization. R. Suriakarthick : Writing – original draft, Methodology, Formal analysis, Conceptualization. V. Gowthami: Conceptualization, Methodology, Data curation, Investigation, Formal analysis Amanullah Fatehmulla: Conceptualization, Validation, Methodology, Funding acquisition, Conceptualization.

Data availability Data will be made available on request.

Declarations

Competing interest The authors declare that they have no known competing financial interests or personal relationships that could have appeared to influence the work reported in this paper.

References

1. R. Hemmati, H. Saboori, Renew. Sustain. Energy Rev. **65**, 11 (2016)
2. N.B. Singh, B. Kumar, U.L. Usman, M.A.B.H. Susan, Nano-Structures Nano-Objects. **39**, 101299 (2024)
3. A. Burke, Appl. Sci. **11**, 8063 (2021)
4. W. Liu, X. Sun, X. Yan, Y. Gao, X. Zhang, K. Wang, Y. Ma, Batteries. **10**, 271 (2024)
5. A.R. Dehghani-Sanij, E. Tharumalingam, M.B. Dusseault, R. Fraser, Renew. Sustain. Energy Rev. **104**, 192 (2019)
6. X. Shen, H. Liu, X.-B. Cheng, C. Yan, J.-Q. Huang, Energy Storage Mater. **12**, 161 (2018)
7. M. Gao, H. Li, L. Xu, Q. Xue, X. Wang, Y. Bai, C. Wu, J. Energy Chem. **59**, 666 (2021)
8. B.D. Fairbanks, L.J. Macdougall, S. Mavila, J. Sinha, B.E. Kirkpatrick, K.S. Anseth, C.N. Bowman, Chem. Rev. **121**, 6915 (2021)
9. D. Xia, J. Quan, G. Wu, X. Liu, Z. Zhang, H. Ji, D. Chen, L. Zhang, Y. Wang, S. Yi, Y. Zhou, Y. Gao, R. Jin, Nanomaterials. **9**, 1225 (2019)
10. Y. Fang, Q. Zhang, L. Cui, Microporous Mesoporous Mater. **314**, 110870 (2021)
11. H. Wang, B. Qi, B. Lu, X. Bo, L. Guo, Electrochim. Acta. **56**, 3042 (2011)
12. S. Chen, W. Xing, J. Duan, X. Hu, S.Z. Qiao, J. Mater. Chem. A **1**, 2941 (2013)
13. G. Wang, L. Zhang, J. Zhang, Chem. Soc. Rev. **41**, 797 (2012)
14. B. Anasori, C. Shi, E.J. Moon, Y. Xie, C.A. Voigt, P.R.C. Kent, S.J. May, S.J.L. Billinge, M.W. Barsoum, Y. Gogotsi, Nanoscale Horizons. **1**, 227 (2016)
15. V.M. Hong Ng, H. Huang, K. Zhou, P.S. Lee, W. Que, J.Z. Xu, L.B. Kong, J. Mater. Chem. A **5**, 3039 (2017)
16. A. VahidMohammadi, J. Rosen, Y. Gogotsi, Science (2021). https://doi.org/10.1126/science.abf1581
17. B. Anasori, Y. Xie, M. Beidaghi, J. Lu, B.C. Hosler, L. Hultman, P.R.C. Kent, Y. Gogotsi, M.W. Barsoum, ACS Nano. **9**, 9507 (2015)
18. R. Xu, C. Wu, H. Xu, Carbon N Y. **45**, 2806 (2007)
19. P. Batys, P. Weroński, M. Nosek, M. Skoczek, Colloids Surf. Physicochem Eng. Asp. **510**, 176 (2016)
20. C.N.R. Rao, K. Gopalakrishnan, U. Maitra, ACS Appl. Mater. Interfaces. **7**, 7809 (2015)
21. B. Weerasuk, T. Chutimasakul, N. Prigyai, T. Sangtawesin, RSC Sustain. **3**, 904 (2025)
22. H. Zheng, Q. Wei, X. Han, X. Yu, Y. Li, J. Zhou, ACS Appl. Nano Mater. **5**, 455 (2022)
23. F. Beck, P. Rüetschi, Electrochim. Acta. **45**, 2467 (2000)
24. J.A. Dowling, K.Z. Rinaldi, T.H. Ruggles, S.J. Davis, M. Yuan, F. Tong, N.S. Lewis, K. Caldeira, Joule. **4**, 1907 (2020)
25. M. Li, R.P. Hicks, Z. Chen, C. Luo, J. Guo, C. Wang, Y. Xu, Chem. Rev. **123**, 1712 (2023)
26. K. Xu, C. Wang, Nat. Energy. **1**, 16161 (2016)
27. G. Ma, A. Zhang, Z. Wang, K. Wang, J. Zhang, K. Xu, Y. Xu, S. Zhou, A. Wang, Mater. Horizons. **12**, 1689 (2025)
28. Z. Xu, K. Yao, Z. Li, L. Fu, H. Fu, J. Li, L. Cao, J. Huang, J. Mater. Chem. A **6**, 10535 (2018)
29. R. Sukanya, M. Hasan, R. Karthik, D. Ranjith Kumar, E. Kamaraj, A. Milton, C. Breslin, J. Lee, J.-J. Shim, Chem. Eng. J. **497**, 154928 (2024)
30. X. Zhu, W. Wang, Z. Cao, S. Gao, M.O.L. Chee, X. Zhang, P. Dong, P.M. Ajayan, M. Ye, J. Shen, J. Mater. Chem. A **9**, 17994 (2021)

31. L. Wang, X. Zhang, Y. Xu, C. Li, W. Liu, S. Yi, K. Wang, X. Sun, Z. Wu, Y. Ma, Adv. Funct. Mater. **31**, (2021)
32. M.A. Kosnan, M.A. Azam, R.F. Munawar, A. Klimkowicz, A. Takasaki, Int. J. Nanoelectron Mater. **17**, 263 (2024)
33. K. Raagulan, R. Braveenth, B.M. Kim, K.J. Lim, S.B. Lee, M. Kim, K.Y. Chai, RSC Adv. **10**, 1613 (2020)
34. M.I.H. Protyai, Bin Rashid Heliyon. **10**, e37030 (2024)
35. L. Zhou, J. Li, C. Xing, Chem. Eng. J. **506**, 159868 (2025)